

Coupling Crustal Seismicity to Crustal Permeability — Empirical Theory for EGS & Hydrothermal Flow Systems

Peter C. Leary, and Peter Malin

Advanced Seismic Instrumentation and Research (ASIR), USA

Abstract: Direct association of natural and induced seismicity with crustal fluid flow properties has long been assumed, particularly for active crustal fault systems, but for a variety of reasons it has been difficult to describe the relationship in terms of subsurface properties. We present microseismicity evidence that, at least in the absence of active faulting, the relationship between microseismicity and crustal permeability can be understood in terms of the spatial correlation empirics of crustal flow properties in a critically-strained brittle crust. In summary, we introduce a theoretic construct in which the observed power-law scaling two-point spatial-correlation property of microearthquake locations, e.g., natural and induced seismicity “clouds”, are direct consequences of spatial fluctuations in crustal permeability controlled by spatially-correlated fluctuations in crustal porosity. A conceptual framework for understanding natural and induced seismicity in terms of the spatially correlated crustal porosity and permeability can significantly improve our ability to interpret microseismicity data in terms of crustal flow structures.

Evidence for a close physical relation between crustal seismicity and crustal permeability is observed at two geothermal developments: (1) large-scale fluid injection at 6 km depth at a Finnish EGS site, and (2) natural seismicity at 3 km depth in an Indonesian geothermal field. Microearthquake locations at both sites show power-law scaling two-point correlation distributions in event separation range r , $\Gamma_{\text{meq}}(r) \sim 1/r^n$, $n \sim 1/2$. Computation shows that the observed microseismicity spatial correlation systematics can be derived from a trio of crustal spatial correlation empirics for crustal porosity ϕ and permeability κ :

- 1) Well-log crustal porosity fluctuation spectral power $P_\phi(k)$ scales inversely with spatial frequency k , $P_\phi(k) \sim 1/k$, for five to six decades of spatial scale length, $\sim 1/\text{km} < k < \sim 1/\text{cm}$;
- 2) In well-core sequences, permeability spatial fluctuations strongly correlate with porosity fluctuations as $\delta \log \kappa \sim \alpha \delta \phi$, with empirical parameter α having values such that $\alpha \phi \sim 3-4$ for rock types spanning two decades of mean porosity, $0.3\% < \phi < 30\%$; the empiric $\alpha \phi \sim 3-4$ guarantees that normally distributed porosity ϕ generates lognormally distributed permeability, $\kappa \sim \exp(\alpha \phi)$;
- 3) For stationary random systems such as plausibly describe the slowly evolving ambient brittle-fracture crust, the Wiener-Khinchin theorem posits a Fourier transform pair for spatially-correlated physical-event distributions $\Gamma(r)$ in offset range r and spatial fluctuation power $P(k)$ in spatial frequency k , $P(k) \sim \int \exp(ikr) \Gamma(r) dr$ and $\Gamma(r) \sim \int \exp(-ikr) P(k) dk$.

Assuming that the ambient crust is in a stationary random process state (in which stochastic parameters such as mean and variance do not change significantly with observation times), we apply the Wiener-Khinchin theorem to numerical simulations of permeability distributions $\kappa(x,y,z)$ for a range of porosity spatial correlations $P_\phi(k) \sim 1/k^m$, $0 < m < 2$, to generate a range of two-point correlation functions $\Gamma_\kappa(r) \sim 1/r^p$ corresponding to the range of porosity spatial correlations. A wide range of numerical simulations show that the observed permeability spatial correlation function $\Gamma_\kappa(r) \sim 1/r^{1/2}$ arises for the porosity spatial-correlation scaling spectral distribution for $m \sim 1$, corresponding to spectral scaling $P_\phi(k) \sim 1/k^1$ that is universally seen in well log data. As it is long recognised that fluid pressure effects promote seismic activity, and as fluid effects are likely to be strongest where permeability is greatest, we logically interpret the observed $\Gamma_{\text{meq}}(r) \sim 1/r^{1/2}$ spatial correlation as corresponding the numerical simulation permeability correlation function $\Gamma_\kappa(r) \sim 1/r^{1/2}$. This correspondence “predicts” that observed seismicity at the EGS and hydrothermal sites is evidence that fundamental ambient crustal rock-fluid interactions physically link crustal porosity ϕ and permeability κ to induced and natural microseismicity.

Our physical interpretation of observed spatial correlation $\Gamma_{\text{meq}}(r) \sim 1/r^{1/2}$ for EGS and hydrothermal system seismicity has two clear practical geothermal applications. It has been extensively demonstrated that shale formations undergoing frack-stimulation emit sustained low-level seismic energy as the formation fluids are disturbed. It has been lately demonstrated that areas of sustained low-level seismic emission can be detected with 10- to 15-meter spatial resolution even before shale formations are drilled or stimulated. Our physical interpretation of microseismicity spatial correlation function $\Gamma_{\text{meq}}(r) \sim 1/r^{1/2}$ provides strong evidence that the demonstrated shale-formation fluid-flow-generated seismic signal generation can be extended to include discrete slip events in magnitude range $-1 < M < 1$ within an ambient stationary crustal state. (In contrast with a stationary ambient crustal state, crustal

volumes undergoing active tectonic faulting are stochastically non-stationary with no expectation that the Wiener-Khinchin theorem applies.) According to our theoretic construct, we can apply the demonstrated shale-formation fluid-flow imaging power to (i) use downhole seismic sensor arrays to monitor the mechanics of EGS permeability stimulation in deep crustal heat exchange volumes, and (ii) use surface seismic array data to map complex flow-connectivity structures in convective geothermal flow systems in order to identify suitable production-well drilling targets with greatly improved (50 meter?) spatial resolution.

Key words: EGS, convective geothermal, permeability stimulation, induced microseismicity, fractures, porosity, permeability

1. Introduction

Systematic spatial correlation of crustal fluid-flow properties over a many decades of scale length is a signature feature of rock-fluid interactions across a wide range of geological settings [1-7]. This paper extends the ambit of fluid-rock interaction spatial correlations to microseismic slip displacements induced by extensive wellbore fluid injection into 6km-deep basement rock [8-9] and to natural microseismicity associated with convective geothermal systems [10]. Relating induced seismicity to spatial correlation properties of crustal fluid flow mechanics has practical implications for two geothermal sectors. First, the spatial correlations observed in crustal stimulation mechanics fuel clear negative implications for standard scenarios of Enhanced/Engineered Geothermal System (EGS) permeability stimulation of basement rock, but at the same time can aid the application of feasible EGS stimulation to extract geothermal energy for district heating plants currently dependent of CO₂-emitting fossil fuels. Second, closely associating induced seismicity with crustal fluid flow structures supports the use of multi-channel ambient seismic noise data to image large-scale flow structures in convective geothermal systems as a means of guiding production-well drilling.

In the following discussion, §2 establishes the vital statistical link between spatial correlations in induced microseismicity and spatial correlations characteristic of crustal fluid-rock interactions in geological media in general and basement rock in particular. In §2.1,

recently observed induced microseismicity at 6 km depth in Fennoscandian basement are contrasted with a standard view of EGS crustal fracture stimulation that ignores spatial correlations. §2.2 attributes the induced seismic event distribution to power-law scaling spatial correlation empirics of crustal fluid-rock interactions seen at all wellbore-accessible depths. §2.3 then uses numerical realisations of §2.2 crustal rock-fluid interaction empirics to derive the observed spatial correlations of induced microseismicity in terms of reactivated fossilised crustal rock-fluid interaction fabric. Speaking mathematically, our numerical modelling “predicts” the observed induced-microseismicity 2-point spatial correlation function $\Gamma_{\text{meq}}(r) \sim 1/r^{1/2}$ from the combination of attested well-log neutron porosity spatial fluctuation power-law spectral scaling $P_{\phi}(k) \sim 1/k^1$ with attested well-core relations between spatially varying porosity ϕ and permeability κ , $\kappa \sim \exp(\alpha\phi)$, $\alpha\phi \sim 3-4$.

The practical implications of §2 induced-microseismicity spatial correlation have for standard EGS stimulation scenarios and for production well drilling for convective geothermal resources are reviewed in §§3-4. On present evidence, it is not clear how naturally occurring wellbore-centric Peclet number $P_e \sim 10$ heat advection can be up-scaled by hypothetical EGS fracture stimulation scenarios to achieve $P_e \sim 100$ levels of heat extraction needed to drive turbines. On the other hand, building on naturally occurring Peclet number $P_e \sim 10$ heat advection offers means to stimulate $P_e \sim 10$ heat advection in long-reach wellbore-centric flow systems for direct use applications. §4 interprets the spatial correlation of ambient microseismicity in hydrogeothermal systems to support prospects for remote-sensing of major

Corresponding author: Peter C. Leary, Ph.D.; research areas/interests: crustal fluid-rock interaction and fracture processes. E-mail: pcl@asirseismic.com.

convective fluid flow structures as targets for production well drilling. Significantly increasing production well success rates at hydrogeothermal sites addresses long-standing investor reluctance to sustain and develop hydrogeothermal resource heat extraction worldwide.

2. Spatially-Correlated Crustal Rock-Fluid Interactions & EGS Permeability Stimulation

Fig. 1 introduces the spatial correlation phenomenology in crustal rock-fluid interactions [1-7]

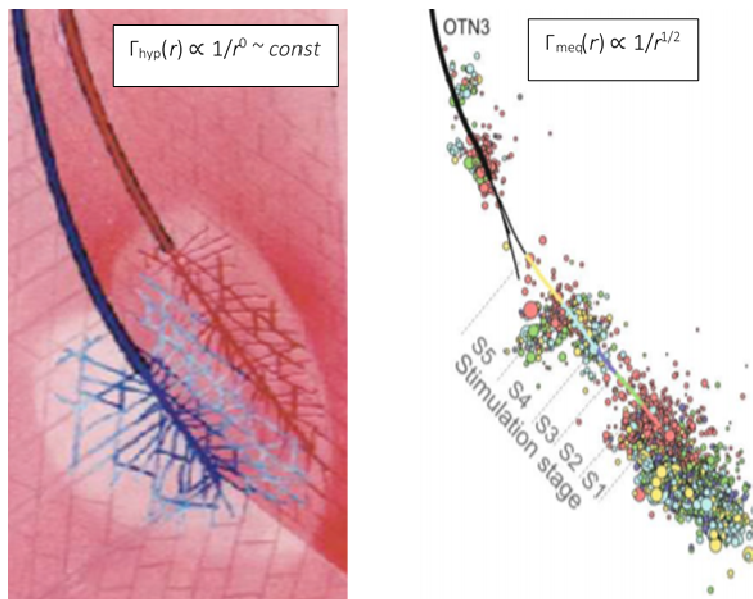


Fig. 1 (Left) Standard hypothetical rock-fluid interaction during wellbore-centric injection of fluid into an EGS crustal heat exchange volume. Blue tints denote cold injected fluid flow that absorbs crustal heat on traversing the heat exchange volume to exit as red-tinted hot fluids at the outtake well. Numerical simulations of the left-hand fluid-rock interaction typically assume that fracture properties such as position, length, width, orientation and aperture are can be represented by uniformly distributed independent random numbers. By the Central Limit Theorem, such numerical constructs lead inevitably to spatially-uncorrelated normally distributed flow property distributions. Any seismicity putatively associated with this hypothetical rock-fluid interaction will have a constant two-point correlation function $\Gamma_{hyp}(r) \propto 1/r^0 \sim const$. (Right) In contrast to the constant statistical correlation function characteristic of standard hypothetical rock-fluid interactions, seismicity induced by wellbore-centric fluid injection is spatially correlated, $\Gamma_{meq}(r) \propto 1/r^{1/2}$, over a decadal range of correlation offsets $30\text{ m} < r < 500\text{ m}$. The power-law nature of the observed 2-point correlation function indicates that the correlation function is scale-independent. Spatially-correlated scale-independent clustering leads to lognormal flow-property distributions as is observed in crustal flow systems worldwide

We distinguish the Fig. 1 hypothetical from the observed fracture distributions via two-point statistical spatial correlation values $\Gamma(r)$ as a function of inter-event spatial offsets r within the crustal

by contrasting direct observation of induced seismicity at depth in basement rock with long-standing but essentially mistaken assumptions about fluid flow through crustal fractures. The left-hand of Fig. 1 illustrates a standard perception of EGS wellbore-centric fluid pressure stimulation of crustal rock [11], while the right-hand details the empirics of microseismicity recently induced by injecting 18000m^3 of water into 6km-deep Fennoscandian basement rock along a 1km length of open wellbore [8-9].

stimulation volumes [12-13; Appendix 1]. The hypothetical distribution of random crustal stimulation fracture events at Fig. 1 left is typically devoid of spatial correlations [14-16; cf. §3]. With no correlation,

the associated microseismicity two-point correlation function is constant, $\Gamma_{\text{hyp}}(r) \propto 1/r^0 \sim \text{const}$. In contrast, the two-point spatial correlation or autocorrelation function for microseismic slip event offsets induced by wellbore-fluid injection in basement rock at Fig. 1 right is seen to be power-law scaling, $\Gamma_{\text{meq}}(r) \propto 1/r^{1/2}$, over a decadal range of inter-event offsets $30 \text{ m} < r < 500 \text{ m}$.

The two-point correlation statistic $\Gamma_{\text{meq}}(r)$ for Fig. 1 induced microseismicity measures the average number of events within a given range, r to $r + dr$, from any given sample event [Appendix 1]. If there is no spatial correlation within a collection of events, then the average number of events at offset interval r to $r + dr$ is independent of offset value r , giving $\Gamma_{\text{hyp}}(r) \propto 1/r^0 \sim \text{const}$. If there is a tendency for fracture-related events to cluster, then the two-point spatial correlation function varies with offset range r in a manner characteristic of the clustering process. The induced seismicity distribution of Fig. 1 (right) shows that stimulation-induced microseismicity slip events in deep basement rock cluster in power-law scaling fashion, $\Gamma_{\text{meq}}(r) \propto 1/r^{1/2}$. In the observed induced seismicity event spatial distribution, sample events systematically tend to be associated with nearer events (smaller r) rather than further events (larger r), and the observed clustering is independent of the inter-event offset, i.e., event clustering occurs without reference to an embedded or structural scale length [1-2]. §2.1 shows that the induced seismicity is independent of which section of the stimulation wellbore injects stimulation fluids, giving evidence that the “stimulated” flow paths are not freshly created at each crustal section but are instead pre-existing fossil flow structures that are reactivated by the injected fluid wherever the injection point. The degree of spatial correlation for the induced seismicity controls the value of the power-law scaling exponent. The scaling exponent is in turn logically determined by the power-law-scaling spatial correlation nature of pre-existing fossil flow structures [1-2]. §2.2 reviews the widely attested pre-existing power-law scaling

nature of well-log porosity fluctuation and its close spatial association with well-core crustal permeability fluctuations at all scale lengths [1-9]. §2.3 discusses how the observed microseismic spatial correlation scaling exponent value $1/2$ is controlled by the pre-existing crustal porosity well-log fluctuation scaling and its associated permeability.

2.1 *Spatial-correlation Phenomenology of Fennoscandian Basement Rock Induced Seismicity*

Over a period of 50 days in June-July 2018, a total of 18000 cubic meters of fresh water were injected at 6km depth into Finnish basement rock at a drill site in the town of Espoo 15 km west of Helsinki. Fluid injection was staged over five nominal 200-meter intervals along a 45-degree deviated open wellbore as sketched in Fig. 2 [8-9].

Seismic monitoring of fluid injection permitted operator control of induced earthquakes during the five-stage sequence of crustal stimulation [8-9]. Seismic monitoring was performed with a 24-station 3C-sensor network (12-station areal near-surface sensor array + 12-station vertical array of sensors at 2-3 km depth). Information on induced-earthquake rates, locations, magnitudes, and evolution of seismic and hydraulic energy-controlled fluid injection; at any stimulation stage, pumping was either stopped or varied between 60-90 MPa wellhead-pressures and 400-800 liter/min flow rates. Over 8000 monitor events were processed within a maximum delay of 5 minutes. Of these, some 6,150 earthquakes with larger signal-to-noise ratios in magnitude range $-1 < M < 1.9$ formed the catalogue for monitoring and evaluating the five-stage fluid injection process.

Fig. 1 (right) shows the cumulative wellbore-centric distribution of induced seismicity for magnitude range $-1 < M < 1.9$ in tight Finnish basement rock. Injection occurred over a 1km open-hole section of wellbore OTN3 at 6km depth. Figs. 3-4 expand the observed induced seismicity distributions for two time-steps during the 50-day stimulation programme [8-9]. The

five 200 m-long fluid injection segments of open OTN3 wellbore in Fig. 1 are marked by different colours — from deepest upward, red/pale green/light green/dark green/purple. Figs. 3-4 show similar induced seismicity distributions over periods of 2 days and 30 days respectively:

- Event distribution is wellbore-centric in depth and azimuth, with no evidence of systematic stress alignment or large-scale fracture fabric sections intersecting the wellbore;
- Event distribution is irregular along the 1 km section of open wellbore, possibly related to fracture fabric variation along the wellbore;

- Events notably cluster above and particularly below the 1km section of open wellbore, indicating that stimulation fluids access crustal volumes not immediately adjacent to wellbore injection intervals;

Event distributions are largely the same regardless of which of the five wellbore intervals is the source of the injected fluid.

From Figs. 3-4, we see that the wellbore-fluid induced stimulation event distributions in one sense agree with the Fig. 1 hypothetical induced seismicity image, while in another sense the rock stimulation event distributions strongly disagree with the details of the hypothetical fracture structure.

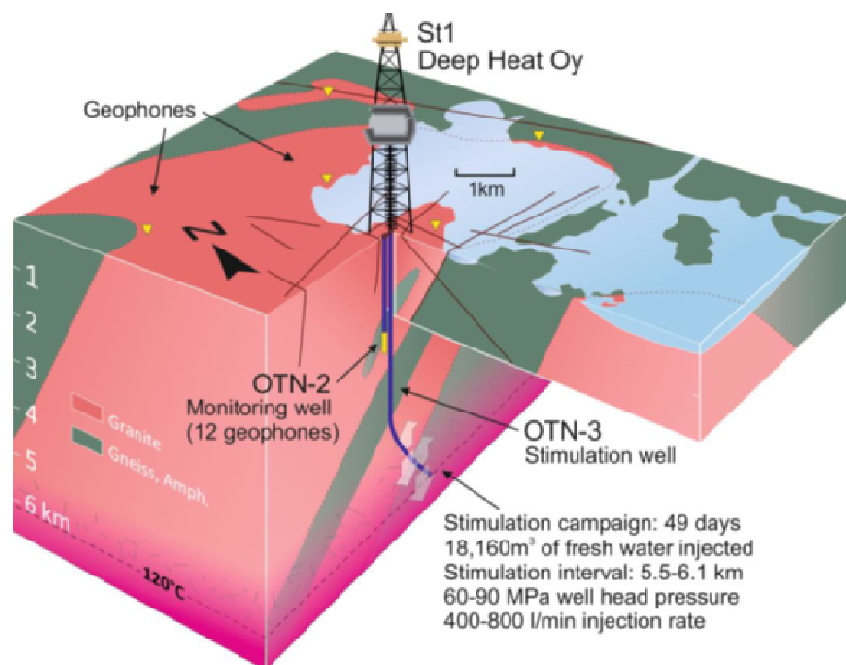


Fig. 2 Sketch of wellbore fluid-injection stimulation project for 6km-deep Finnish basement crustal volume enclosing a 1km-long 45° deviated open section of wellbore OTN3. Successive fluid injection episodes occurred at 5 nominal 200 m stages in the 1km open wellbore over a 50-day span in June-July 2018. An areal array of 12 near-surface borehole sensors and a 12-module sensor array at 2-to-3 km depth in wellbore OTN2 monitored seismic activity induced by fluid injection. Close monitoring of induced seismic event locations and magnitudes allowed control of fluid injection pressures and rates [8-9].

The Fig. 1 hypothetical fracture distribution without spatial correlations is generically understood to imply that stimulation fluids generate or reactivate a fracture network that is more or less the same without regard to the precise location of the injection wellbore within the crustal stimulation volume [11; §3]. When crustal rock is assumed to be spatial-correlation free, all that

matters is a mean fracture density, which by hypothesis does not vary significantly within the crustal volume. Hence there is an implicit expectation that an induced hypothetical fracture network will be more or less the same, regardless of where the stimulation wellbore is located. In this sense, the Fig. 1 hypothetical fracture construct can be said to be consistent with the Fig. 1

Coupling Crustal Seismicity to Crustal Permeability — Empirical Theory for EGS & Hydrothermal Flow Systems

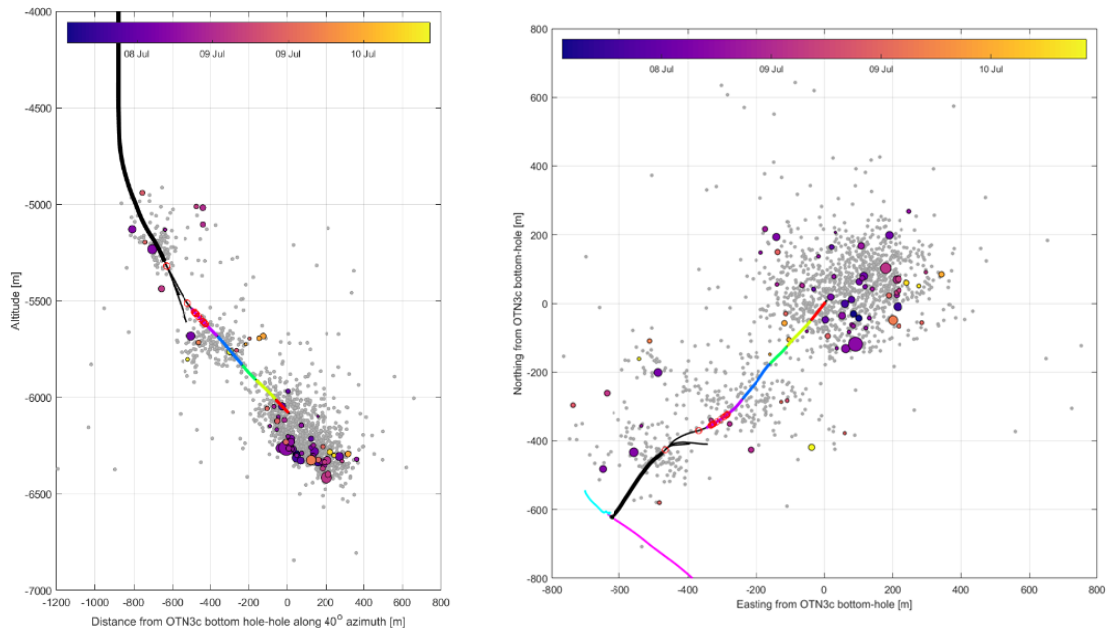


Fig. 3 Coloured dots locate induced seismicity events in time interval 08-10 July 2018 against a backdrop of cumulative event locations in grey. The active injection interval during 08-10 July was the fourth stimulation section (dark green). Prior and later injection intervals contributed to the cumulative distribution in grey. Despite the considerable number of grey events spatially proximate to the fourth stimulation interval, and the considerable number of induced events elsewhere in the stimulation volume, no induced events occur immediately adjacent to the dark green stimulation interval as would be expected by standard views of crustal wellbore-centric stimulation.

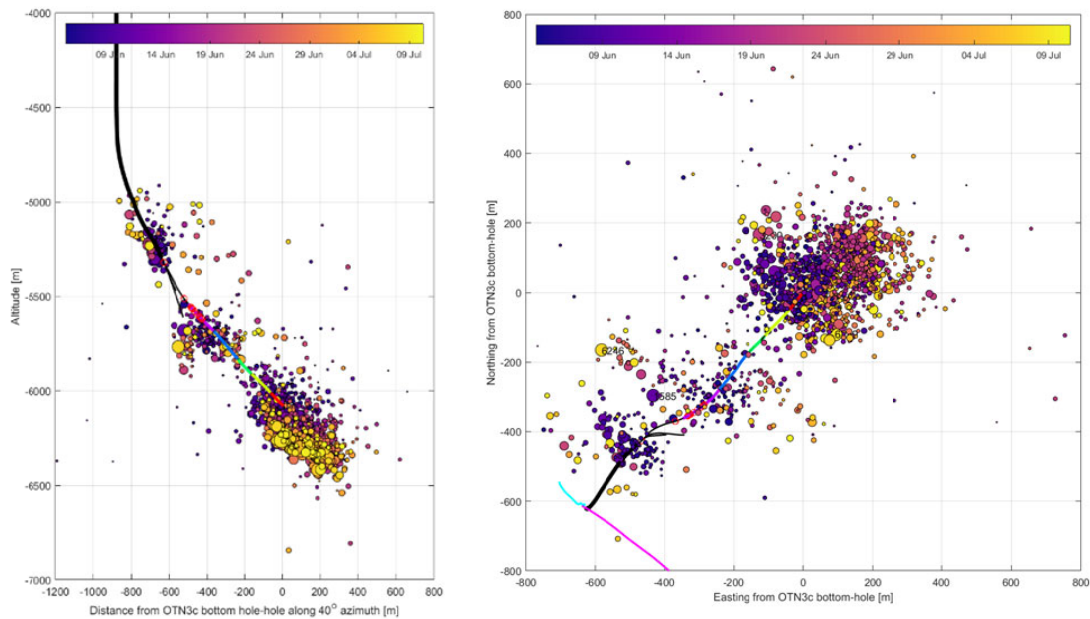


Fig. 4 Coloured dots locate induced seismicity events across the 30-day interval 09 June to 09 July 2018. In this period, fluid was injected into the crustal stimulation volume from the first four of the five 200 m-long open well injection intervals (red, pale green, light green, dark green). As in Fig. 3, induced seismicity occurs essentially in the same stimulation/cluster pattern regardless of where in the 1km-long open wellbore the fluid is injected. A majority of induced seismicity occurs below the toe of the open wellbore for all four open wellbore stimulation intervals, with a sizeable cluster of stimulation events located above the open wellbore stimulation interval. Most particularly, there is no evidence that induced seismicity is proximate to the injection interval; all four injection intervals are seen to stimulate seismic activity in the same set of crustal volume clusters.

observed stimulation event distributions, which are largely the same regardless of which stimulation interval injects the fluid.

On the other hand, Figs. 3-4 show a clear discrepancy between the Fig. 1 hypothetical and observed stimulation fracture configurations. While it doesn't overly matter where the OTN3 open hole stimulation occurs in the accessed crustal volume, the spatial distribution of induced events is materially different from that expected for the hypothetical stimulation.

The seeming paradox of simultaneous similarity and dissimilarity between Fig. 1 hypothesis and observation is easily resolved by noting that in both cases we can presume that the crustal fracture fabric is pre-existing, with fluid injections merely activating, or reactivating, a pre-existing fracture fabric. In both hypothetical and observation cases, the specific pre-existing crustal fracture fabric in the stimulation volume is expected to be revealed by stimulation microseismicity.

In light of Figs. 1 and 3-4, our question becomes, what is the pre-existing fracture fabric of crustal rock? Is the pre-existing fracture fabric spatially uncorrelated as in Fig. 1 (left) or spatially-correlated as in Fig. 1 (right)?

The answer is abundantly clear: vast arrays of well-log, well-core, and well-productivity data [1-7] show that the inherent pre-existing fracture fabric of crustal rock is that of Fig. 1 (right) spatial correlation, not that of Fig. 1 (left) spatial non-correlation. In essence, Fig. 1 induced microseismicity data show that the standard hypothetical fracture fabric and its numerical realisations by means of uncorrelated random numbers are simply wrong. Examining crustal spatial correlation evidence in greater detail establishes that the power-law scaling spatial correlation empirics for crustal fluid-rock interaction yield the observed Fig. 1 power-law scaling induced seismicity spatial correlation function $\Gamma_{\text{meq}}(r) \sim 1/r^{1/2}$.

2.2 Generic Crustal Poroperm Spatial Correlation Generated by Steady-State Tectonic Crustal Deformation

Evidence for a “correct” spatial correlation formulation for crustal fluid-rock interaction that generates a pre-existing fracture-connectivity fluid flow fabric that imposes spatial correlations on induced seismicity as seen in Figs. 1, 3, 4, can be summarised as:

- 1) Well-log porosity fluctuation power that scales inversely with spatial frequency k , $P_{\phi}(k) \sim 1/k$, over five decades of spatial scale length, $1/\text{km} < k < 1/\text{cm}$ [1-2];
- 2) Well-core sequences showing that spatial variations in the logarithm of crustal permeability $\log k$ are closely associated with spatial variations in crustal porosity ϕ , $\delta \log k \sim \alpha \delta \phi$, with the product $\alpha \phi$ of mean porosity and empirical parameter α having a narrow range of values, $3 < \alpha \phi < 4$, over two decades of mean porosity value, $0.3\% < \phi < 30\%$ [3-7];
- 3) For stationary random physical systems, spatial correlation distributions $\Gamma(r)$ that relate to spectral fluctuation power distributions $P(k)$ via Fourier transformation, $P(k) \sim \int \exp(ikr) \Gamma(r) dr$ (Wiener-Khinchin theorem) [17; Appendix 2].

In Figs. 5-6, well-log and well-core data from the 9 km-deep KTB science well [6] demonstrate the well-log spectral empiric (I) and well-core poroperm empiric (II) for crystalline basement rock to 6km depth. Figs. 7-8 use empiric (III) to connect empirics (I)-(II) to induced and natural microseismicity.

The overarching crustal context for Figs. 5-6 is steady-state tectonic deformation acting on fluid-saturated porous rock comprised of tough mineral grains bonded by weak cements [1-7]. Steady-state tectonic deformation at strain rates of order $10^{-8}/\text{yr} < \dot{\epsilon} < 10^{-7}/\text{yr}$ [21-22] over 10^4 - 10^5 -year intervals generates crustal strains of order $10^{-4} < e < 10^{-2}$. Tectonic strains of this order introduce irreversible finite strain damage at weak cements bonding strong mineral grains [18-20].

The essentially universal well-log spectral systematics of Fig. 5 show that on-going tectonic deformation creates in the brittle-fracture crust a wide-sense stationary random grain-scale fracture connectivity that is spatially correlated at across 6 decades of scale length, $mm < \ell < km$. In particular, as indicated in Fig.

5, crustal well-logs of neutron porosity in basement rock record spatial fluctuations that persist to 6km depth with Fourier spectral power scaling inversely with spatial frequency, $S_{\phi}(k) \sim 1/k$, over scale range $1/km < k < 1/m$.

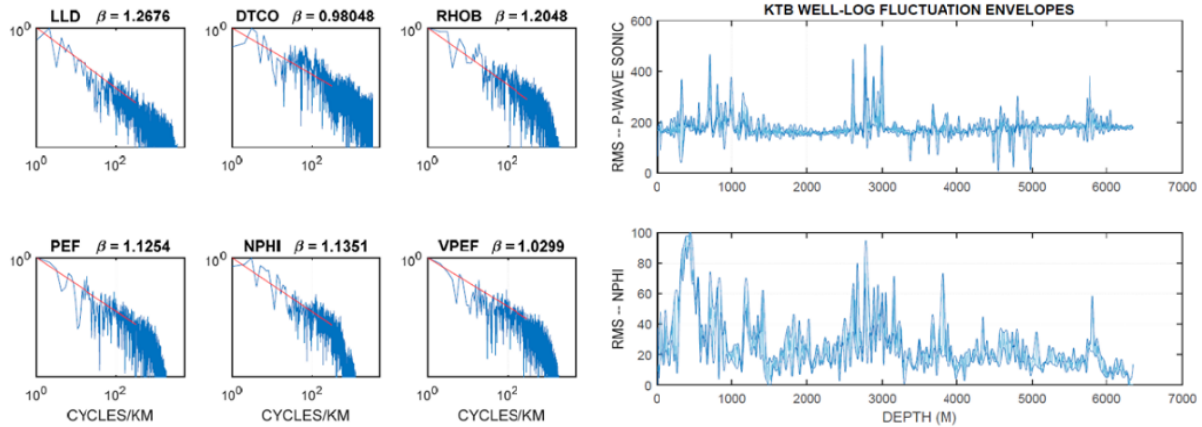


Fig. 5 (Left) Log-log plots of KTB well-log Fourier power-spectral scaling $P(k) \sim 1/k^\beta$ for spatial fluctuation in six physical variables measured between 4-6 km depths in crystalline basement (LLD = lateral log induction; DTCO = P-wave sonic velocity; RHOB = mass density; PEF = photoelectric absorption; NPHI = neutron scattering \equiv porosity; VPEF = weighted photoelectric absorption); plot title numbers give value of power-law scaling exponent β fit to fluctuation power-spectra ; well-log ensemble mean exponent is $\beta \sim 1.12 \pm 0.1$ over spatial frequency range $1 \text{ cycle/km} < k < 300 \text{ cycles/km}$. (Right) Amplitude of P-wave sonic and neutron porosity spatial fluctuations as a function of depth in KTB main well; well-log fluctuation amplitudes of spectral to left do not significantly reduce with depth in crustal rock [6].

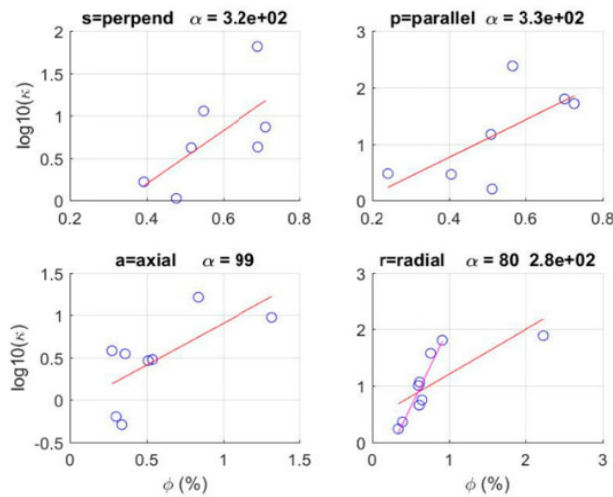


Fig. 6 Open circles give well-core poroperm data for 31 KTB core between 4 and 6 km depths [6]. Red lines fit to plotted poroperm relation $\log(\kappa) \propto \alpha\phi$. Plots are for different core axis directions relative to wellbore axis and local rock fabric axis (s = perpendicular to fabric; p = parallel to fabric; a = along wellbore axis; r = perpendicular to wellbore axis). Aside from a single well-core poroperm outlier, poroperm data conform to a linear relation $\log(\kappa) \propto \alpha\phi$ with proportionality constant having values of order $\alpha \sim 300$ with mean value $\alpha_{\phi} \sim 3$ for mean basement porosity $\phi \sim 1\%$. For observed poroperm proportionality constants $3 < \alpha_{\phi} < 4$, integrating relation $\log(\kappa) \propto \alpha\phi$ over reservoir-scale poroperm sequences gives observational constraint (II) expression $\kappa \sim \exp(\alpha\phi)$. For $3 < \alpha_{\phi} < 4$, normal distributions of porosity $0 < \phi < 0.3$ guarantee that reservoir-scale crustal permeability κ distributions are lognormal, as observed worldwide in groundwater, hydrocarbon, geothermal, and fossilized crustal reservoir fluid systems [25-28].

The essentially universal presence of $1/k$ -spectral-scaling of empiric (I) comprehensively refutes the standard assumption that crustal porosity in geological formations is effectively determined throughout the formation by a mean value and standard deviation that can be determined by a handful of small-scale samples [23-24]. Further, as seen in Fig 6, rather than formations having a mild quasi-uniform porosity and permeability in a formation, porosity fluctuations at all scale lengths throughout geological formations generate strongly fluctuating spatial connectivity between pores at all scales as per crustal empiric (II). The associated empirical value $\alpha\phi \sim 3-4$ guarantees lognormal distributions of well-productivity, as observed worldwide [25-28].

Fig. 6 illustrates that the connection between porosity and permeability observed in reservoir rock worldwide [3-7] extends to crystalline rock at 4-6 depth. Generic irreversible grain-scale finite strain damage is naturally greatest where porosity is greatest. Spatially-correlated grain-scale fracture connectivity thus constitutes a generic rock-fluid interaction that generates the spatially erratic fluid percolation fluid pathways observed at all scales in the drillable crust. In particular, Fig. 6 illustrates well-core poroperm data for porosities $< 1\%$, showing that crustal permeability κ in basement rock at depth is described by spatially-correlated porosity ϕ , $\kappa \sim \exp(\alpha\phi)$, for α an empirical parameter. The observed values of α are such that the exponent product term $\alpha\phi$ has a fixed mean value, $\alpha\phi \sim 3-4$ [7]. For all observed ranges of parameter values α , crustal permeability $\kappa \sim \exp(\alpha\phi)$ is formally a lognormal distribution, as observed for crustal well-flow productivity distributions worldwide [25-28].

The multi-decadal duality of spatial frequency and spatial range empirics (I)-(II) gives rise to the third spatial correlation empiric (III), by which correlated random fluctuations in space $\Gamma(r)$ relate to spectral fluctuation power distributions in spatial frequency $P(k)$ as a Fourier transformation duality, $P(k) \sim$

$\int \exp(ikr)\Gamma(r)dr$ with its inverse transform $\Gamma(r) \sim \int \exp(-ikr)P(k)dk$ [17; Appendix 2]. Insofar as the random distribution in a physical system is stationary in a wide sense, i.e., the physical system mean-values and their fluctuation bounds do not change in during physically relevant times, then the Fourier power-spectrum $P(k)$ of a physical fluctuation sequence is equivalent to the spatial correlation function $\Gamma(r)$ of that fluctuation sequence.

2.3 Two-point Spatial Correlation for Induced Seismicity in Crust with Spatially-Correlated Rock-Fluid Interactions

Empirics (I)-(II) enable us to numerically simulate crustal poroperm fields ϕ and $\kappa \sim \exp(\alpha\phi)$ in 2 or 3 dimensions for a range of spectral power-law scaling exponents $0 < m < 2$, $S_{\phi}^m(k) \sim 1/k^m$. Number field representations with $m \sim 0$ correspond to essentially uncorrelated spatial fluctuations in porosity (as is routinely assumed for hydrocarbon reservoir characterisation [23-24]). At the other spatial correlation extreme, number field representations with $m \sim 2$ correspond to essentially highly correlated spatial fluctuations in porosity such as layered media (layers have step-function structure for which the Fourier power spectra scale inversely with the square of the spatial frequency, $S(k) \sim 1/k^2$ [17]). Accordingly, we can use such numerical representations of porosity fields ϕ and associated permeability fields $\kappa \sim \exp(\alpha\phi)$ to compute the resulting spatial correlation function $\Gamma^m(r)$ as a function of exponent m used to generate a range of spatially correlated porosity fields ϕ . As we can expect that power-law scaling spatial correlation fields $S_{\phi}^m(k) \sim 1/k^m$ generate a power-law spatial correlation functions, we can numerically evaluate the correlation function exponent n for spatial correlation form $\Gamma^m(r) \propto 1/r^n$ in the associated permeability number fields.

As we cannot log crustal permeability in the same way we can log crustal porosity, we look to induced seismicity to measure the spatial correlation property

of crustal permeability. To make contact with induced seismicity data, we can expect that spatial domains of higher/lower porosity ϕ and associated permeability $\kappa \sim \exp(\alpha\phi)$ correspond to spatial domains with higher/lower likelihood of seismic slip. To test this expectation, we check if the spatial correlation property of Figs. 1, 3, 4 observed induced microseismicity has the same spatial correlation function as our numerical constructs for the highest values of porosity ϕ and associated permeability $\kappa \sim \exp(\alpha\phi)$.

To this end, consider a class of 3D numerical distributions of crustal permeability with generalised poroperm spectral correlation properties based on crustal rock-fluid interaction empirics (I)-(II). The generalised 3D numerical permeability fields are controlled by porosity spectral scaling according to $S_\phi(k) \sim 1/k^m$ for spectral scaling exponent $0 < m < 2$. Within this range of generalised 3D permeability fields, we find the consequent range of two-point spatial correlation functions of form $\Gamma^m(r) \propto 1/r^n$, where exponent n is to be found by inspection of the numerical correlation distribution generated for by values of $0 < m < 2$.

Fig. 7 shows representative result of such a numerical exercise. For a set of numerical parameters with normally distributed 3D porosity field $0.1 < \phi < 0.3$ distributed across a data cube of 300 nodes on a side, the 3D permeability field is computed for proportionality constant in $\log(\kappa) \sim \alpha\phi$ set to $\alpha = 20$ with a mean product parameter $\alpha\phi \sim 5$. The mean values and deviations of the corresponding 2-point spatial correlation exponents $n(m)$ given by $\Gamma^m(r) \propto 1/r^{n(m)}$ are determined for incremental steps 0.2 for power-law spatial correlation exponent m between 0.1 and 1.8, $m = 0.1:0.2:1.8$ over 10 layers of $Z = 30$ units each the 3D data volume.

Fig. 7 summarises a large number of data simulations for varying numerical parameters, showing that the numerical exercise stably fixes the 2-point spatial correlation exponent $n \sim 1/2$ for porosity spatial correlation exponent $m \sim 1$, $\Gamma^{m \sim 1}(r) \propto 1/r^{n \sim 1/2}$. Our

numerical experiment thus agrees with the Fig 1 empirical observation for wellbore fluid injection induced seismicity at 6km depth in basement rock conditioned by rock-fluid interaction empirics (I)-(II).

Fig. 8 compares an observed spatial distribution of Figs. 1, 3, 4 induced seismicity events (left) with a representative numerical realisation of Fig. 7 permeability distributions for correlation exponents $m \sim 1$ and $n \sim 0.64$ (right). The numerical realisation (right) has no spatial errors associated with observed microseismicity data and thus better exhibits the fine-scale spatial correlations that location errors in induced seismic event data (left) do not have. Both the observed numerical simulation event distributions have power-law scaling dependency on interevent range r , and the scaling exponent for interevent range is the same $n \sim 0.5-0.6$ for both observation and numerical models.

Figs. 7-8 numerical constructions indicate that the Figs. 1, 3, 4 observed induced seismicity spatial correlation $\Gamma^{m \sim 1}(r) \propto 1/r^{n \sim 1/2}$ responds to naturally occurring spatial correlation embodied in crustal rock-fluid empirics (I)-(III). We thus conclude that spatial correlations evident in the EGS stimulation-induced microseismicity reflect a fundamental spatial-correlation phenomenology in crustal rock-fluid interactions. This spatial-correlation phenomenology is essentially ignored in historical approaches to EGS stimulation [11] and has little impact on assessing the meaning of microseismicity in convective geothermal flow systems [10].

3. EGS Stimulation for AD HOC Fracture-Flow Models without Spatial Correlation

Standard EGS fracture-borne fluid flow stimulation scenarios that are designed to achieve heat extraction needed to produce electrical power from the drillable crust heat store draw heavily, even exclusively, on the spatial averaging practices of hydrocarbon reservoir management. Mathematically, spatial averaging of

reservoir flow heterogeneity produces physically realistic models only if the random fluctuations in reservoir flow processes are statistically independent — if, that is, flow properties at a reservoir formation

location X are unrelated to or uncorrelated with flow properties at all neighbouring formation locations Y at all scales [5, 23-24].

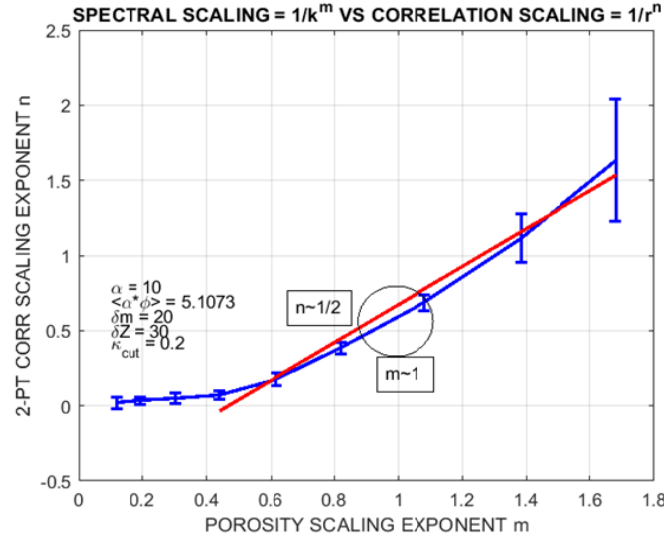


Fig. 7 Representative numerical relationship between degree of power-law scaling spatial correlation of 3D porosity field given by exponential parameter $0 < m < 2$, $S_\phi(k) \sim 1/k^m$, and degree of power-law scaling 2-pt spatial correlation function exponent n , $\Gamma^m(r) \propto 1/r^n$, determined for permeability field $\kappa(:) \sim \exp(\alpha\phi(:))$. If it is assumed that the locations of highest porosity and permeability correspond to the mostly likely locations of induced seismicity slip events, then the numerical constructions “predict” that for observed porosity fluctuation power scaling exponent $m \sim 1$, the associated induced seismicity has 2-point correlation function scaling exponent, $\Gamma^{m-1}(r) \propto 1/r^{n-1/2}$, in agreement with the observation of Fig. 1 (right).

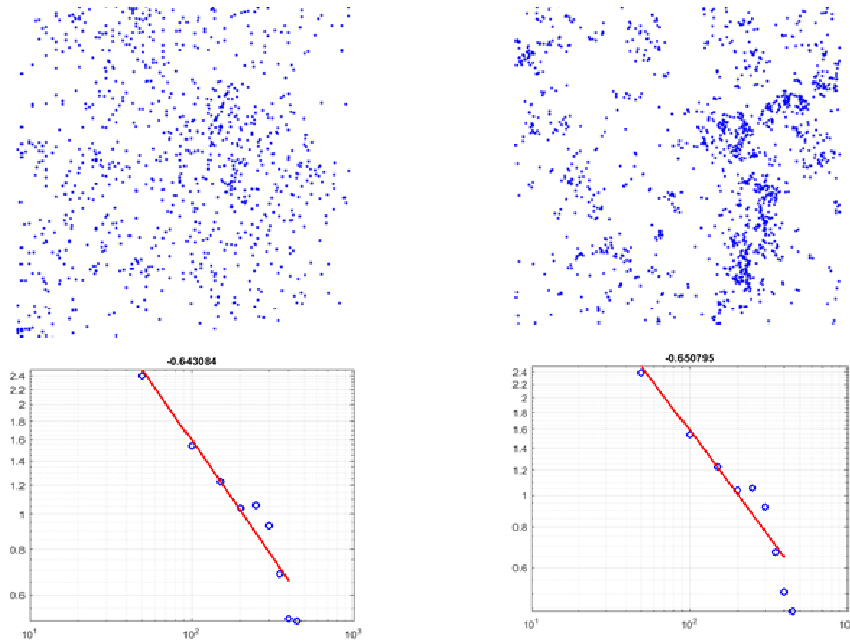


Fig. 8 (Left) Representative spatial distribution and resultant 2-point correlation function for Fig. 1 (right) induced seismicity at 6 km depth in crystalline basement. (Right) Representative spatial distribution and resultant 2-point correlation function for numerical simulation of empirical crustal porosity and permeability distributions described in text. There is a strong likelihood that the different degrees of fine-scale local clustering for field data (left) and simulation data (right) is due to limited spatial resolution of field data.

While the spatial non-correlation concept of reservoir heterogeneity is highly implausible in light of abundant well-log and well-core spatial-correlation empirics (I)-(II), and the use of empiric (III) to associate microseismicity spatial correlation with empirics (I)-(II), there are at least four aspects of hydrocarbon reservoir management that appear to collectively override the inherent implausibility in interests of hydrocarbon production commercial practice:

- 1) large numbers of wells over which to perform spatial averages;
- 2) low cost of wells relative to the price of produced fluid – i.e., drilling more wells is a safe option for unreliable statistical predictions of well production distributions;
- 3) high probability that wells pay for themselves over a production life – i.e., even if lognormal well production distributions mean a majority of wells produce a minority of hydrocarbons while a minority of wells produce a majority of hydrocarbons, low producing wells are nonetheless profitable;
- 4) well management issues focus on the immediate vicinity of the wellbore, i.e., the “skin effect” — rather than on long-range well-to-well interactions.

Applying hydrocarbon-reservoir management and cost aspects that define well performance by spatial

averaging over the production field does not, however, match geothermal production well cost profile:

- 1) geothermal resources are serviced by an order of magnitude fewer wells, significantly reducing the statistical significance of spatial averaged well performance;
- 2) geothermal wells cost two orders of magnitude more than hydrocarbon wells per unit price of produced fluid – i.e., geothermal production wells are a much larger operational cost burden than are hydrocarbon production wells;
- 3) successful geothermal production wells flow at one to two orders of magnitude higher rate than hydrocarbon wells, greatly reducing the success rate of geothermal wells and greatly increasing the cost burden of geothermal wells relative to hydrocarbon wells;
- 4) geothermal wells respond to crustal conditions over one or two orders of magnitude larger radii than do hydrocarbon wells; in particular, EGS wellbores need to be systematically stimulated over long reaches of open hole to generate wellbore-to-wellbore flow across an enclosing heat exchange crustal volume, a process that offers no statistical basis for spatial averaging.

Table 1 highlights the scale of disparity between crustal reservoir formation spatial averaging practice as applied to hydrocarbon production and to geothermal energy production.

Table 1 Impact ratios for spatial averaging of flow heterogeneity for geothermal over hydrocarbon production wells.

Well Property	Hydrocarbon	Geothermal	G/H Impact Ratio
Number of wells	High – Hundreds per field	Low – Tens per field	10
Well cost relative to pay	Low – \$50-\$100 per barrel	High – \$0.5-\$1 per barrel	100
Well success	High – even low flow wells pay	Low – only high flow wells pay	10-100
Well environment	Local (skin effect ~ 1 m-3 m)	Non-local (> 30 m-300 m)	30-100

In light of Table 1 impact of reservoir heterogeneity on geothermal wells relative to hydrocarbon wells, we focus how single or EGS doublet geothermal wells actually (rather than hypothetically) interact with crustal flow heterogeneity revealed by empirics (I)-(II)

as supplemented by the use of empiric (III) applied to observed EGS stimulation microseismicity. Focusing on how wellbores interact with the actual crustal flow properties shows the impact of the conceptual flaws that affect many or most EGS permeability stimulation

scenarios that have been advanced for generating electrical power from drillable crust heat store. Table 1 also hints that hydrocarbon well spatial averaging practice may have discouraged exploration for effective means of locating production well sites in convective hydrogeothermal fields; §4 outlines one such means that emerges from the §2 discussion of observed microseismicity spatial correlations.

Conventional EGS stimulation scenarios characterise fractures as essentially uniform discontinuities in an otherwise “effectively uniform” elastic medium. Residual flow property heterogeneity is, by hypothesis, “effectively” eliminated by spatial averaging. Application of spatial averaging to reservoir formations appeared unquestioned in the early flow models, which drew directly on the mathematics of thermal conduction [29]. Attempts to formalise the practice of spatial averaging were made by Hubbert [30-31] and by Bear [32]. With spatial averaging a prevailing concept, many schemes were advanced to incorporate fractures into spatially-averaged flow scenarios. Fig. 9 illustrates two standard approaches, both categories of which “fracture-as-discontinuity” approximations persisting over a 50-year period. At left, fluid velocity in fractures is approximated by Poiseuille-Hagen cubic law flow, $V[\text{m/s}] \sim g[\text{Pa/m}] \cdot h^3[\text{m}^3]/12 \cdot \mu[\text{Pa} \cdot \text{s}]$, or close variants accounting for fracture roughness [33-36]. At right Darcy flow through a “double porosity” medium features a high-porosity/high-permeability material that is systematically embedded with uniform blocks of

low-porosity/low-permeability material. Double porosity, effectively introduced by Warren & Root in 1963, was incorporated in Tough2, the oldest, most widely used flow simulation code [37-40].

True to their origin in the spatial-averaging conceptual framework, Fig. 9 “fracture as discontinuity” flow model computations are implemented using uncorrelated random numbers [41-43]. As such, the Central Limit Theorem mathematically insures that the resultant model flow distributions are normally distributed [23-24] rather than, say, the lognormal distribution routinely observed worldwide [25-28].

Considering the large number of diverse Fig. 9-type flow models appearing as EGS stimulation scenarios, it is convenient to focus our wellbore-centric discussion on a recent computational exercise that dispenses with any pretence at physical accuracy in favour of a thin uniform permeability flow structure [44]. Fig. 10 (left) sketches the computational model crustal heat exchanger as rectangular prism. The prism, $\sim 1\text{km}$ thick and extending $\sim 4\text{km}$ laterally and $\sim 3\text{km}$ vertically, is designed to be large enough to sustain 35MW of electrical power production for 30 years. The key model feature, Zone 5, is a 1m-thick planar vertical layer of uniform permeability $\kappa \sim 10^{-11} \text{m}^2$ (10 Darcy) serving as a generic flow structure for carrying fluid from injection wells to production wells. Fig. 10 (right) gives three examples of Fig. 9-type well-fracture intersections that indicate how the Zone 5 fluid transport structure might be conceived in relation to actual crustal fractures.

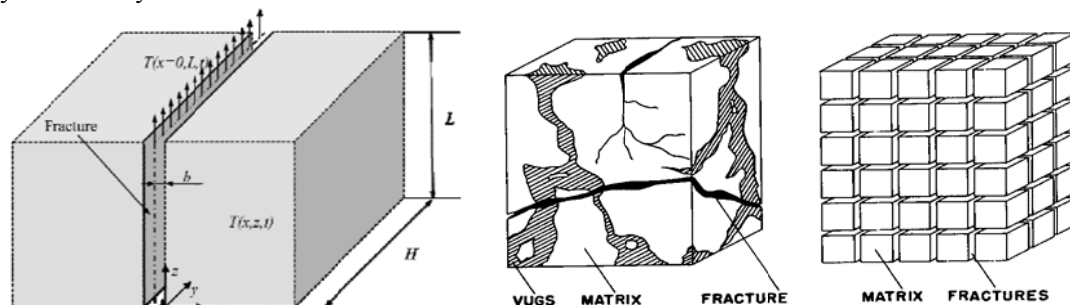


Fig. 9 (Left) Illustration of by Poiseuille-Hagen planar flow approximation to fluid flow in fractures; fluid velocity is given as $V[\text{m/s}] \sim g[\text{Pa/m}] \cdot h^3[\text{m}^3]/12 \cdot \mu[\text{Pa} \cdot \text{s}]$, where the pressure gradient g is constant along both axes the fracture plane [33-36]. (Right) Double porosity approximation to a block of heterogeneous crust introduced by Warren and Root, and later incorporated into the widely used Tough2 flow simulation code [37-40].

Computation with the Fig. 10 (left) flow structure shows that the heat exchange prism maximises heat extraction efficiency for input and outtake wells separated by 2 km flowing at rate $V \sim 100$ L/s. Expressing wellbore thermal heat production as $Q_{th} = VT\rho C$ calibrates the generic well-pair flow performance for a given model crustal temperature T for water with volumetric heat capacity $\rho C \sim 4\text{MJ/m}^3$. For model wellbore-to-wellbore flow rate $V \sim 100\text{L/s}$ and bottom hole temperature $T = 80^\circ\text{C}$, the heat produced is $Q_{th} \sim 30\text{MW}$.

While the hypothetical Fig. 10 $Q_{th} \sim 30\text{MW}$ EGS heat exchanger simply ignores wellbore interfaces to the surrounding crust, we learn from the §2 EGS induced seismicity distribution how the crustal fluid-rock interaction fabric actually responds to wellbore fluid injection. Rather than passing smoothly into a uniform high-permeability planar flow structure, actual injection fluids enter crustal rock via reactivated heterogeneous fossil spatially-correlated fracture-connectivity channels. Taking the opposite approach of Fig. 10, we focus on the mechanics of radial fluid flow ϕv_0 at the wellbore interface by expressing volumetric flow V in terms wellbore radius r_0 along a wellbore length ℓ , $V = 2\pi r_0 \phi v_0 \ell$. The associated advection heat transfer Peclet number given by ϕv_0 is $P_e = r_0 \phi v_0 / D = r_0 \phi v_0 \rho C / K$, where rock-fluid thermal diffusivity $D = K / \rho C = 2.7/862/4510 \sim 0.7 \cdot 10^{-6} \text{m}^2/\text{s}$.

If we treat Fig. 10 thermal heat flow as occurring over wellbore length $\ell \sim 200\text{m}$ at crustal temperature $T_0 = 80^\circ\text{C}$, the effective Fig. 10 Peclet number is $P_e = Q/2\pi K \ell T_0 = 30 \cdot 10^6 / 2\pi / 200 / 80 / 2.7 \sim 100$. For comparison, Peclet numbers observed for fluid transport in actual crust are occasionally $P_e \sim 10$ but generally $P_e < \sim 1$ [5, 6].

Building on well-log data for a 2km deep well in Fennoscandian crustal basement associated with Fig. 1 EGS stimulation data, Fig. 11 evaluates Peclet number $P_e \sim 10$ heat transport flow for naturally occurring crustal fracture structures [6]. The computed wellbore-centric flow distribution for a 20 m-cube of

crust is shown in Fig. 11 (left). Peclet numbers for wellbore-centric radial flow at meter-scale stages along the wellbore axis are shown in the middle plots for analytic fits (red) to the model radial temperature distributions (blue). The resultant model axial temperature field shown as the red trace in Fig. 11 (right) is constrained by the observed wellbore axial temperature profile in black. The agreement between model and observed temperature profiles validates the computation performed using the empirical rock-fluid interaction heterogeneity (I)-(II), and indicates that naturally occurring wellbore-centric crustal advective flow systems can have Peclet numbers of order $P_e \sim 10$ but are generally of order $P_e < \sim 1$.

With Fig. 11 calibrating actual wellbore-centric advective flow at order $P_e \sim 10$ or less, and §2 microseismicity indicating that injected fluids enter the crust surrounding a stimulation wellbore by activating pre-existing fossil flow fracture-connectivity pathways, we see that standard EGS stimulation measures can probably generate intervals of $P_e \sim 10$ wellbore-centric advective flow. It follows, however, that in order for actual wellbores to achieve Fig. 10 hypothetical EGS wellbore advection heat transfer, every meter of a 200-meter wellbore length associated with Fig. 10 has to be stimulated to permeability 10 to 100 times the naturally occurring distribution of advective flow permeability.

Further, while Fig. 11 refers to naturally occurring fracture structures feeding the wellbore over a 10-meter radius, Fig. 12 shows that realising a Fig. 10 EGS stimulation scenario requires wellbores to be stimulated to radii of several hundred meters. Fig. 12 shows a formal solution to wellbore-centric radial heat transport, and as such gives approximate stimulation radii required to sustain wellbore-to-wellbore heat advection in a crustal heat exchange volume for heat extraction times up to 30 years at heat extraction rates $2 < P_e < 50$ [5,6].

Figs. 9-12 compare a standard EGS flow stimulation scenario for $P_e \sim 100$ heat production needed for

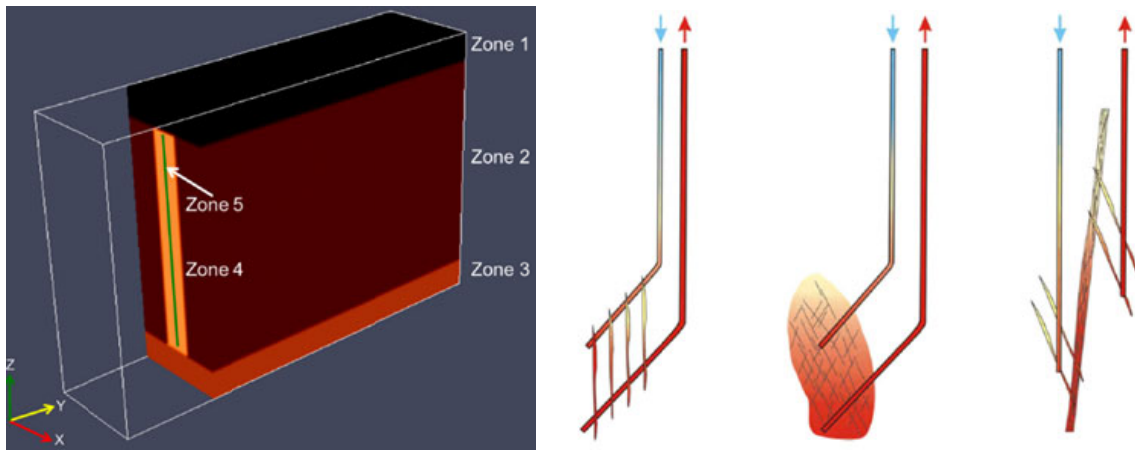


Fig. 10 (Left) Generic crustal heat exchange model for producing 35 MW of electrical energy [44]; the principal model feature is Zone 5, a 1-meter thick layer of uniform permeability extending 4 km laterally and 3 km vertically. (Right) Examples of wellbore-fracture intersections that, for computational simplicity, are replaced by the Zone 5 permeability layer [44].

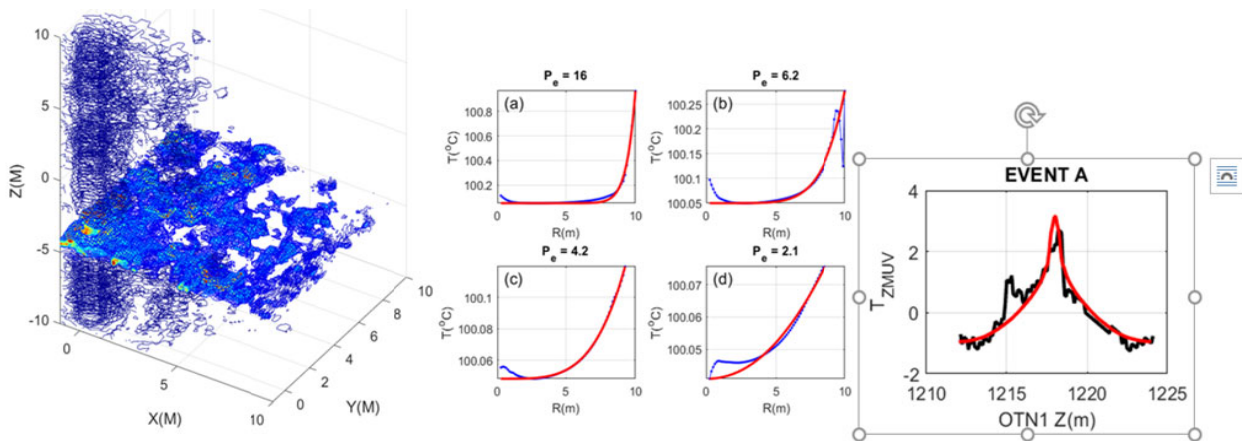


Fig. 11 (Left) Model of a m -thick planar permeability flow structure of $\kappa \sim 0.02$ Darcy leaking crustal fluid into a wellbore at hydrostatic pressure. (Mid) Model radial temperature profiles (blue) for four axial levels at 1m intervals along the wellbore from the planar flow structure matched by 2D analytic radial profiles (red) with Peclet number given above each plot. (Right) Resultant axial temperature field (red) fit to observed temperature along the wellbore axis (black). Data/model from [6; cf. 5].

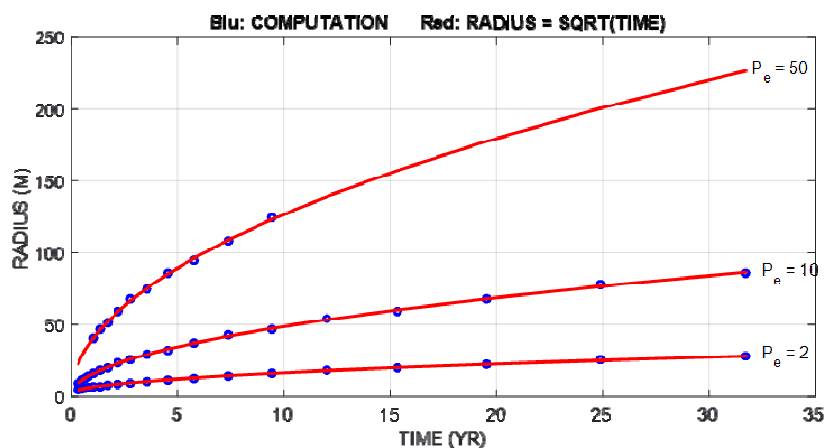


Fig. 12 Wellbore-centric stimulation radii (vertical axis) needed for wellbore-to-wellbore heat exchange flow volume to sustain heat extraction for given time periods (horizontal axis) for given Peclet number extraction rates 2, 10 and 50 [5, 6].

electrical power general with naturally occurring wellbore-centric $P_e \sim 10$ heat production. As the naturally occurring heat production can be computed for widely validated rock-fluid interaction empirics (I)-(III) applied to temperature distributions in an actual crustal wellbore, we need not resort to hypothetical physical processes for wellbore stimulation. Rather, we can see from the wellbore-specific data in Figs. 1, 3, 4 and §2 that EGS-type crustal flow stimulation follows an unruly path that is closely conditioned by pre-existing fossilised flow structures occurring irregularly and unpredictably along the wellbore. Fig. 11 indicates that within the population of fossil flow paths, a few wellbore intervals show occasional residually-active flow structures with localised $P_e \sim 10$ transport capability, while most of the wellbore is characterised by $0 < P_e < 1$ advective flow capability. It follows from close inspection of actual wellbore-centric flow and heat transport processes that Fig. 10 and related hypothetical $P_e \sim 100$ levels of EGS stimulation scenarios are very far from detailed observational support.

4. Ambient MEQ Spatial Correlation Evidence for Convective Geothermal Flow Imaging

Given the §2 association of power-law-scaling spatial correlation of EGS basement rock induced microseismicity with pre-existing crustal permeability distributions due to power-law-scaling spatially-correlation porosity distributions, it is of interest to look at ambient microseismicity distributions at convective hydrogeothermal sites. Available well-log and well-core data, though sparse, show that convective geothermal flow systems are characterised by the same power-law-scaling spatial correlation empirics (I)-(II) as are observed worldwide [45]. It is thus plausible that ambient microseismicity at convective flow sites [10] has the same power-law-scaling spatial correlation property as

observed for in §2 EGS basement rock induced seismicity. Connecting ambient microseismicity distribution statistics with the statistics of convective geothermal flow permeability structures opens the door for using ambient seismicity data to accurately locate significant flow structures of a convective geothermal flow system as targets for production well drilling [46-50].

Fig. 13 summarises the ambient microseismicity recorded at a geothermal field in west-central Java, Indonesia [10]. A total of 877 microseismicity event locations occur in three groups. In parallel with the Fig. 8 displays of Fig. 1 event planar distribution (left) and computed permeability event distribution (right), the upper plots of Fig. 13 show the planar distributions of two microseismicity spatial clusters associated with steam production in the geothermal field. The Fig. 13 event clusters have, left and right respectively, 337 and 365 events; the remaining 175 microseismicity events are either associated with a deep lying structural fault or are diffusely scattered at the near-surface.

In parallel with Fig. 8 processing of observed EGS and computed microseismicity distributions, the 2-pt spatial-correlation functions given in Fig. 13 lower plots are evidence of systematic event spatial correlation within the microseismicity associated with the local steam field fluid flow system. As with Fig. 8, the log-log plot format associates a straight-line fit to the data with a power-law exponent describing the statistical clustering across a 200-1000 meters scale range (for inter-event offsets > 1 km, the event populations become too sparse to return robust estimates). For the 200-1000 m event-offset range, the two geothermal field microseismicity clusters give power-law scaling spatial correlation exponents consistent with the $\Gamma_{\text{meq}}(r) \sim 1/r^{1/2}$ function observed in the §2 induced seismicity event population and its §3 interpretation in terms of crustal permeability distributions.

From the observational and computational evidence of §§2-4, crustal rock-fluid interaction empirics (I)-(II)

combined with the Fourier transform duality (III) can be understood to be generic properties of crustal flow systems. We are thus invited to view the present basement rock and convective geothermal system evidence for systematic microseismicity spatial correlations as being part of a larger suite of generic crustal properties. Continuing in this vein, we can note

the considerable evidence that hydrofracture stimulation of shale formation hydrocarbons excites low-level seismicity specific to fluids flowing in fracture-connectivity pathway, and that this flow-specific seismicity can be systematically detected by processing multi-channel surface seismic data acquired over shale formations [46-50].

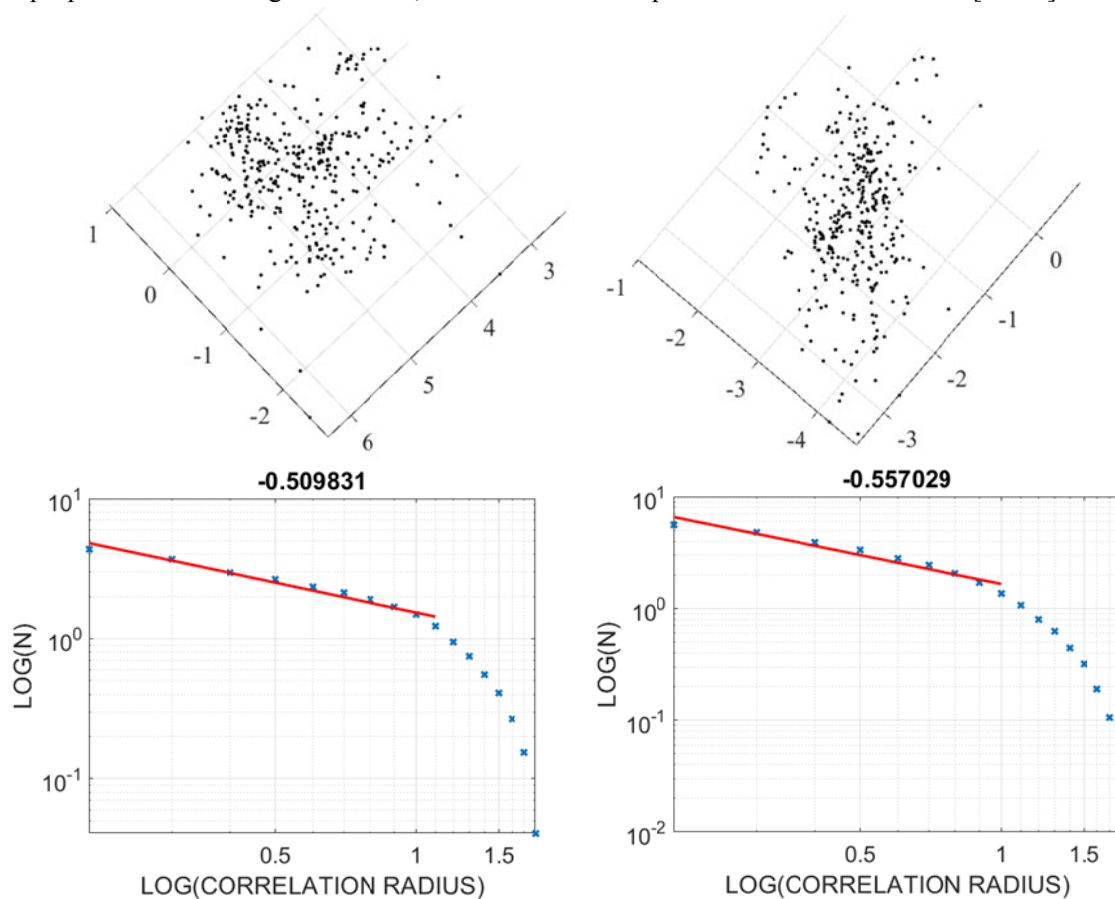


Fig. 13 (Upper plots) Horizontal planar sections of microseismicity event distribution at an Indonesian convective geothermal field [10]. (Lower plots) Two-point spatial correlation functions (blue x's) for above planar event distributions showing power-law scaling fits across event-to-event offset range 200-1000 meters (red). Power-law scaling exponents in plot titles show the geothermal field ambient microseismicity is consistent with the §2 spatial correlation function $\Gamma_{\text{meq}}(r) \sim 1/r^{1/2}$ derived from spatial correlation empirics (I)-(II) of generic basement crust. Associating spatially-correlated ambient microseismicity with inherent permeability heterogeneity in convective geothermal flow systems supports use of detailed low-level microseismicity maps to locate major flow structures as targets for production well drilling [46-50].

Fig. 14 shows graphic evidence of multi-channel surface seismic detection of low-level flow structures within an activated shale formation. Prior to any shale formation stimulation, the ambient seismic noise field recorded above a shale formation domain was processed to reveal the series of fracture-connectivity flow pathways denoted by red lines. When the

horizontal wellbore denoted by the straight black line started to inject water into the pre-existing fracture-connectivity structures, a patch of localized seismicity was observed at the intersection of the wellbore and flow structure (leftmost panel). With continued wellbore fluid injection, the local fracture-connectivity structure activated fluid

movement in increasingly widespread fracture-connectivity structures as signaled by seismic emission throughout the previously mapped fracture-connectivity structures (2nd, 3rd, and 4th panels).

Detection of low-level seismicity associated with fluid flow in a generic crustal volume implies a generic ability to map low-level ambient microseismicity generated in geothermal reservoir flow structures. Using accurate surveys of geothermal section seismic velocity structures, it should be possible to detect and process small but persistent ambient noise signals to map fracture-connectivity flow structures to ~ 50-meter spatial accuracy. Much or most current convective geothermal field surveys are subject to

low-resolution spatial averaging structure mapping [10]. Spatially averaged flow structure surveys, with, say, spatial resolution ~ 500 meters (comparable to 40-acre gridding of hydrocarbon reservoirs), provide little guidance for drilling production wells. Inadequate flow structure data is particularly acute in the earlier stages of reservoir development, leading to costly “learning curve” drilling of many unproductive wells. Fig. 14 evidence for extending crustal flow heterogeneity empirics (I)-(II) to convective geothermal systems clearly indicates that ability of multi-channel seismic data to reliably locate major convective flow channels to, say, 50 m resolution will greatly improve the economics of geothermal field production well drilling.

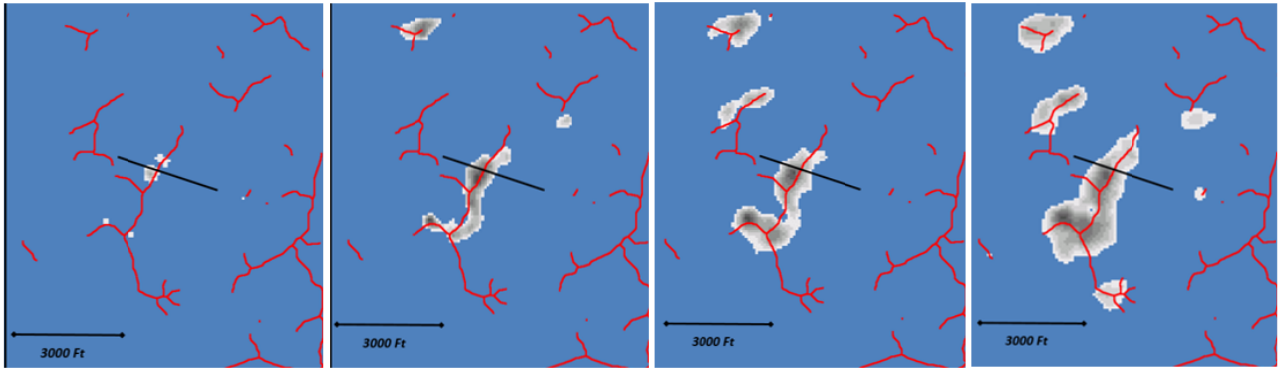


Fig. 14 Time sequence of low-level seismic energy emission (progressive white areas) in a Barnett shale formation due to fluid injection at a horizontal wellbore (black line) where it intersects a fracture-connectivity structure (red lines). The population of red lines denoting fracture-connectivity flow structures was mapped using surface-seismic-array data recorded prior to wellbore fluid injection. Shale formation sedimentary crustal sections can be accurately imaged by 3D seismic-reflectivity data to provide an accurate crustal velocity model. Shale formation fracture connectivity structures can be resolved to 15-meter accuracy [46-50].

5. Conclusions

Well-log and well-core spatial correlation empirics for crustal poroperm properties — (I) crustal porosity fluctuation power scaling inversely as a power-law in spatial frequency k , $P_\phi(k) \sim 1/k$, and (II) spatial variations in crustal permeability κ associated with crustal porosity ϕ , $\kappa \sim \exp(\alpha\phi)$ — lead to high degrees of spatial heterogeneity in crustal flow structures attested over a wide range of geological settings. Observation of spatial correlation systematics for microseismicity event locations, $\Gamma_{\text{meq}}(r) \sim 1/r^{1/2}$,

associated with EGS stimulation of deep basement rock (§2) and convective geothermal flow (§4), can be modelled using numerical representations of crustal empirics (I)-(II) and connected to microseismicity distributions by the Wiener-Khinchin theorem (III). Observational evidence that EGS induced seismicity is spatially correlated directly and comprehensively refutes most or all present-day scenarios for electrical power production requiring stimulation of Peclet number $Pe \sim 100$ heat extraction volumes in the deep crust. Rather, present evidence indicates that inherent crustal flow heterogeneity is compatible with

stimulation of $P_e \sim 10$ heat extraction volumes for direct use. Observation of microseismicity spatial correlation systematics $\Gamma_{\text{meq}}(r) \sim 1/r^{1/2}$ over convective geothermal systems indicates that flow-structure generation of low-level ambient seismicity validated by shale formation stimulation data processing has the potential to accurately locate high-volume flow structures within convective flow systems. Significantly enhancing production well drilling precision significantly reduces geothermal field development and operating costs.

References

- [1] P. C. Leary, Rock as a critical-point system and the inherent implausibility of reliable earthquake prediction, *Geophysical Journal International* 131 (1997) 451-466.
- [2] P. C. Leary, Fractures and physical heterogeneity in crustal rock, in: J. A. Goff, & K. Holliger (Eds.), *Heterogeneity of the Crust and Upper Mantle — Nature, Scaling and Seismic Properties*, Kluwer Academic/Plenum Publishers, New York, 2002, pp. 155-186.
- [3] P. C. Leary and F. Al-Kindy, Power-law scaling of spatially correlated porosity and log(permeability) sequences from north-central North Sea Brae oilfield well core, *Geophysical Journal International* 148 (2002) 426-442.
- [4] P. Leary, J. Pogacnik and P. Malin, Fractures ~ Porosity --> Connectivity ~ Permeability --> EGS Flow Stimulation, in: *Proceedings 36th Geothermal Resources Council 36th Annual Conference*, Reno NV, 30 Sep.-3 Oct., 2012.
- [5] P. Leary, P. Malin and R. Niemi, Fluid flow & heat transport computation for power-law scaling poroperm media, *Geofluids*, 2017, available online at: <https://doi.org/10.1155/2017/9687325>.
- [6] P. C. Leary, P. E. Malin, T. Saarno and I. Kukkonen, Prospects for assessing enhanced geothermal system (EGS) basement rock flow stimulation by wellbore temperature data, *Energies*, 2017, doi: 10.3390/en10121979.
- [7] P. Leary, P. Malin, T. Saarno and I. Kukkonen, $\alpha_{\text{eq}} \sim \alpha_{\text{crit}}$ — Basement rock EGS as extension of reservoir rock flow processes, in: *Proceedings 43rd Workshop on Geothermal Reservoir Engineering*, Stanford University, Stanford, California, February 12-14, 2018, SGP-TR-213.
- [8] G. Kwiatek, T. Saarno, T. Ader, F. Bluemle, M. Bohnhoff, M. Chendorain, G. Dresen, P. Heikkinen, I. Kukkonen, P. Leary, M. Leonhardt, P. Malin, P. Martínez-Garzón, K. Passmore, P. Passmore, S. Valenzuela and C. Wollin, Controlling Fluid-Induced Seismicity during a 6.1-km-Deep Geothermal Stimulation in Finland, AGU Abstract ID and Title: 403801; Abstract Number: S21A-0, 2019.
- [9] G. Kwiatek, T. Saarno, T. Ader, F. Bluemle, M. Bohnhoff, M. Chendorain, G. Dresen, P. Heikkinen, I. Kukkonen, P. Leary, M. Leonhardt, P. Malin, P. Martínez-Garzón, K. Passmore, P. Passmore, S. Valenzuela and C. Wollin, Controlling Fluid-Induced Seismicity during a 6.1-km-deep Geothermal Stimulation in Finland, *Science*, 2019.
- [10] V. A. Muchlis, R. Sule, A. D. Nugraha and Y. Kusnadi, Reservoir characterization based on hypocenter location analysis and 3-D seismic velocities, in: *Proceedings World Geothermal Congress*, Melbourne, Australia, 19-25 April 2015.
- [11] J. W. Tester et al., *The Future of Geothermal Energy: Impact of Enhanced Geothermal Systems (EGS) on the United States in the 21st Century*, Massachusetts Institute of Technology and U.S. Department of Energy Report, Idaho National Laboratory, INL/EXT-06-11746, 2006.
- [12] Y. Y. Kagan and L. Knopoff, Spatial distribution of earthquakes: the two-point correlation function, *Geophys. J. R. astr. Soc.* 62 (1980), 303-320.
- [13] L. D. Landau and E. M. Lifshitz, *Statistical Physics*, Pergamon Press, Oxford, 1958.
- [14] Renard Ph and de Marsily G., Calculating equivalent permeability: A review, *Advances in Water Resources* 20 (1997) (5-6) 253-278.
- [15] A. J. Katz and A. H. Thompson, Quantitative prediction of permeability in porous rock, *Physical Review B* 34 (1986) (11), available onlien at: <https://link.aps.org/doi/10.1103/PhysRevB.34.8179>.
- [16] X. Zhang, D. J. Sanderson, R. M. Harkness and N. C. Last, Evaluation of the 2-D permeability tensor for fractured rock masses, *Int. J. Rock Mech. Min. Sci. & Geomech.* 33 (1996) (1) 17-37.
- [17] R. N. Bracewell, *The Fourier Transform and Its Applications*, McGraw-Hill, New York, 2000, p. 122.
- [18] B. C. Trent and L. G. Margolin, A numerical laboratory for granular solids, *Engineering Computations* 9 (1992) 191-197.
- [19] H. Yin and J. Dvorkin, Strength of cemented grains, *Geophysical Research Letters* 21 (1994) 903-906.
- [20] J. Dvorkin, A. Nur and H. Yin, Effective properties of cemented granular materials, *Mechanics of Materials* 18 (1994) 351-366.
- [21] Y. Hamiel, O. Katz, V. Lyakhovskiy, Z. Reches and Y. Fialko, Stable and unstable damage evolution in rocks with implications to fracturing of granite, *Geophysical Journal International* 167 (2006) 1005-1016.
- [22] T. J. Craig, E. Calais, L. Fleitout, L. Bollinger and O. Scotti, Evidence for the release of long-term tectonic strain stored

- in continental interiors through intraplate earthquakes, *Geophysical Research Letters* 43 (2016) 6826-6836.
- [23] R. A. Crovelli, Probability and Statistics for Petroleum Resource Assessment, USGS Open-File Report 93-582, 1993, available online at: <https://pubs.er.usgs.gov/publication/ofr93582>.
- [24] M. Rouaud, Probability, Statistics and estimation — Propagation of uncertainties in experimental measurement, *Creative Commons Attribution 2.5*, 2017.
- [25] P. Malin, P. Leary, E. Shalev, J. Rugis, B. Valles, C. Boese, J. Andrews and P. Geiser, Flow Lognormality and Spatial Correlation in Crustal Reservoirs: II—Where-to-Drill Guidance via Acoustic/Seismic Imaging, in: *Proceedings of the World Geothermal Congress 2015*, Melbourne, Australia, 2015.
- [26] G. Gustafson, Strategies for groundwater prospecting in hard rocks: A probabilistic approach, *Norges geologiske undersøkelse Bulletin* 439 (2002) 21-25.
- [27] D. Banks, P. Gundersen, G. Gustafson, J. Makela and G. Morland, Regional similarities in the distributions of well yield from crystalline rocks in Fennoscandia, *Norges geologiske undersøkelse Bulletin* 450 (2010) 33-47.
- [28] D. G. Krige, Lognormal de Wijsian geostatistics for ore evaluation, South African Institute of Mining and Metallurgy, Johannesburg, South Africa, 1981.
- [29] C. V. Theis, The relation between the lowering of the piezometric surface and the rate and duration of discharge of a well using ground-water storage, *Trans. Am. Geophys. Union*, 1935; Muskat M., *The Flow of Homogeneous Fluids through Porous Media*, McGraw-Hill: New York, NY, USA, 1937, p. 763.
- [30] M. K. Hubbert, *Motion of Ground Water*, *Trans. N. Y. Acad. Sci.* 3 (1941) 39-55.
- [31] M. K. Hubbert, Darcy's law and the field equations of the flow of underground fluids, *Int. Assoc. Sci. Hydrol. Bull.* 2 (1957) 23-59.
- [32] J. Bear, *Dynamics of Fluids in Porous Media*, American Elsevier: New York, NY, USA, 1972.
- [33] R. W. Zimmerman and G. Bodvarsson, Hydraulic conductivity in rock fractures, LBL-35976 UC-800, 1994.
- [34] S. Sisavath, A. Al-Yaarubi, C. C. Pain and R. W. Zimmerman, A simple model for deviations from the cubic law for a fracture undergoing dilation or closure, *PAGEOPH* 160 (2003) 1009-1022.
- [35] R. W. Zimmerman, The history and role of the cubic law for fluid flow in fractured rocks, in: *Proceedings of the Session H071 Dynamics of Fluids and Transport in Fractured Porous Media*, San Francisco, CA, USA, 3-7 December 2012.
- [36] D. Sutter, D. B. Fox, B. J. Anderson, D. L. Koch, P. R. von Rohr & J. W. Tester, Sustainable heat farming of geothermal systems: A case study of heat extraction and thermal recovery in a model EGS fractured reservoir, in: *Proceedings 36th Workshop on Geothermal Reservoir Engineering*, Stanford University, 31 January-2 February 2011.
- [37] J. E. Warren and P. J. Root, The behavior of naturally fractured reservoirs, *Society of Petroleum Engineers Journal* (1963) 245-255.
- [38] K. Pruess, C. Oldenburg and Moridis, TOUGH2 User's Guide, Version 2.1, Tech. Rep. LBNL-43134, Lawrence Berkeley National Laboratory, 2012.
- [39] K. Pruess, The TOUGH Codes — A Family of Simulation Tools for Multiphase Flow and Transport Processes in Permeable Media MS 90-1 1 16, LBNL, 2003.
- [40] T. Arbogast, Jr. J. Douglas and U. Hornung, Derivation of the double porosity model of single phase flow via homogenization theory, *Siam J. Math. Anal.* 21 (1990) (4) 823-836.
- [41] Q. Lei, J. P. Latham and C. F. Tsang, The use of discrete fracture networks for modelling coupled geomechanical and hydrological behaviour of fractured rocks, *Computers and Geotechnics* 85 (2017), doi: <http://dx.doi.org/10.1016/j.compgeo.2016.12.024>.
- [42] Y. F. Alghalandis, D. Elmo and E. Eberhardt, Similarity Analysis of Discrete Fracture Networks, 2017, arXiv:1711.05257.
- [43] D. Elmo, S. Rogers, D. Stead and E. Eberhardt, Discrete Fracture Network approach to characterise rock mass fragmentation and implications for geomechanical upscaling, *Journal Mining Technology, Transactions of the Institutions of Mining and Metallurgy* 123 (2014), doi: [doi:doi.org/10.1179/1743286314Y.0000000064](https://doi.org/10.1179/1743286314Y.0000000064).
- [44] C. Jain, C. Vogt and C. Clauser, Maximum potential for geothermal power in Germany based on engineered geothermal systems, *Geothermal Energy* (2015), doi: [10.1186/s40517-015-0033-5](https://doi.org/10.1186/s40517-015-0033-5).
- [45] P. Leary, P. Malin, E. Shalev, G. Ryan, C. Lorenzo and M. Flores, Lognormally distributed K/Th/U concentrations — Evidence for geocritical fracture flow, los azufres geothermal field, MX, *Geothermal Resources Council Transactions* Vol 37, Las Vegas, Nevada, USA, 29 September - 2 October 2013.
- [46] P. Geiser, J. Vermilye, R. Scammell and S. Roecker, Seismic used to directly map reservoir permeability fields, *Oil & Gas Journal* 104 (2006) 46.
- [47] P. Geiser, A. Lacazette and J. Vermilye, Beyond “dots in a box”: An empirical view of reservoir permeability with tomographic fracture imaging, *First Break* 30 (2012).
- [48] P. Leary, P. Malin and Starr, Physics-based sampling of lognormal reservoir well production/productivity distributions, *37th NZ Geothermal Workshop*, 18-20 November 2015, Taupo, New Zealand.

[49] C. Sicking, J. Vermilye and A. Yaner, Forecasting reservoir performance by mapping seismic emissions, *Interpretation* 5 (2017) (4), doi: doi.org/10.1190/INT-2015-0198.1.

[50] J. Ross, K. Parrott, J. Vermilye and A. Klaus, Tomographic fracture imaging: Examples of induced fracture and reservoir-scale observations during wellbore stimulations, Niobrara and Bakken plays, USA, *The Leading Edge*, 2017, doi: doi.org/10.1190/tle36050437.1.

Appendix 1 Matlab Two-Point Correlation Function Computation

```
% [corrfun r rw] = twopointcorr( x,y,dr)   Developed by Ilya Valmianski   email: ivalmian@ucsd.edu
% Computes the two-point correlation function over a 2D lattice of a fixed width and height
% x - list of x coordinates of points   y - list of y coordinates of points   dr - binning distance for successive circles
% corrfun – two-point correlation function   r – radial values for coordfun   rw - number of particles for particular r
value
% Low rw means corrfun is unreliable at that r.
%
function [ corrfun r rw] = twopointcorr( x,y,dr)
    x = reshape(squeeze(x),[length(x) 1]); y = reshape(squeeze(y),[length(y) 1]);
    % real height/width; number particles; largest radius
    width = max(x)-min(x); height = max(y)-min(y); totalPart = length(x); maxR = sqrt((width/2)^2 + (height/2)^2);
    %r bins, area bins   default blksize = 1000
    r = dr:dr:maxR; av_dens = totalPart/width/height; rareas = ((2*pi*r* dr)*av_dens); blksize = 1000;
    corrfun = r*0; rw = r*0; % allocate space for corrfun/rw
    numsteps = ceil(totalPart / blksize); % number of steps to be considered
    for j = 1:numsteps % loop through all particles, compute correlation function
        indi = (j-1)*blksize+1; indf = min(totalPart,j*blksize);
        [corrfunArr   rwArr] = arrayfun(@   (xj,yj)
onePartCorr(xj,yj,x,y,r,rareas),x(indi:indf),y(indi:indf),'UniformOutput',false);
        rw = rw + sum(cell2mat(rwArr),1); corrfun = corrfun + sum(cell2mat(corrfunArr),1);
    end
    corrfun = corrfun ./rw;corrfun = corrfun(rw~=0); r = r(rw~=0);rw = rw(rw~=0); % truncate values with no
contributions
end
%
function [corrfun rw] = onePartCorr(xj,yj,x,y,r,rareas) % compute radii in (xj,yj)-centered coordinates
    rho=hypot(x-xj,y-yj);rho=rho(logical(rho))';
    maxRho = min([max(x)-xj,xj-min(x),max(y)-yj,yj-min(y)]); % compute maximum unbiased rho
    rho=rho(rho<maxRho); % truncate to highest unbiased rho
    rw=r*0; rw(r<maxRho)=1; % indicate for which r-values correlation function is computed
    count=histc( rho,[-inf r]); count=count(2:end); % compute count with correct binning
    corrfun = count./rareas; % normalize density
end
```

Appendix 2 Expression of the Wiener-Khinchin Theorem

If $f(x)$ has the Fourier transform $F(s)$, then its autocorrelation function $\int_{-\infty}^{\infty} f^*(u) f(u+x) du$ has the Fourier transform $|F(s)|^2$.

Derivation:

$$\begin{aligned} \int_{-\infty}^{\infty} |F(s)|^2 e^{i2\pi xs} ds &= \int_{-\infty}^{\infty} F(s) F^*(s) e^{i2\pi xs} ds \\ &= f(x) * f^*(-x) \\ &= \int_{-\infty}^{\infty} f(u) f^*(u-x) du \\ &= \int_{-\infty}^{\infty} f^*(u) f(u+x) du. \end{aligned}$$

Fig. A2.1 Consider a real mathematical function $f(s)$ describing a physical spatial or temporal sequence, e.g., a crustal well-log. The mathematical function $f(s)$ can be random but it is bounded and continuous. By the above derivation excerpted from [17, p122], the physical sequence $f(s)$ has Fourier transform $F(k) \equiv \int ds f(s) \exp(i2\pi ks)$, with power spectrum $|F(k)|^2$ that is mathematically equivalent to the sequence autocorrelation $\Gamma(s) \equiv \int dr f(r) f(s+r)$. If the physical process generating sequence $f(s)$ is scale-independent, then the Fourier spectrum is power-law, $F(k) \sim 1/k^\beta$. For scale-independent random physical processes, if the process is spatially or temporally *uncorrelated*, the power-law scaling exponent is zero, $\beta = 0$, and the physical process is termed *white or Gaussian noise*. If the random physical process is spatially or temporally *strongly correlated*, $\beta = 2$, the physical process is termed *Brownian noise*. Intermediate spatial or temporal correlation, $\beta = 1$, characteristic of well-log sequences worldwide [1-2], generates *pink noise* or *1/f-noise*. By the Wiener-Khinchin theorem, the corresponding autocorrelation function is power-law, $\Gamma(s) \sim 1/s^m$. Numerical simulations of spatially-correlated random fluctuations show that for *pink noise* or *1/f-noise* crustal porosity distributions, the associated spatial autocorrelation function for crustal permeability has exponent $m \sim 1/2$, $\Gamma(s) \sim 1/s^{1/2}$.